Acta Mech 224, 2559–2575 (2013)
DOI 10.1007/s00707-013-0885-3

Phoevos K. Koukouvinis · John S. Anagnostopoulos · Dimitris E. Papantonis

Simulation of 2D wedge impacts on water using the SPH–ALE method

Received: 30 October 2012 / Revised: 21 January 2013 / Published online: 27 April 2013

Abstract Prediction of the forces on pitching boat hulls is a subtle issue, since the underlying phenomena are highly dynamic and unsteady. The solution of a full 3D model of the hull is possible, but comes with a high computational cost; alternatively, it might be simpler to assume the hull as consecutive 2D slices. The traditional CFD approach, with mesh-based algorithms, introduces additional complexity due to mesh motion and interface tracking. By adopting a Lagrangian point of view, the computational algorithm would be substantially simpler, since free surface and moving geometries would be handled easily. In the current work, the smoothed particle hydrodynamics meshless method is used within an arbitrary Lagrangian–Eulerian framework (SPH–ALE), in order to predict the force and motion of a wedge during high-velocity water entry. Various impacts have been simulated, using wedges of different shapes and masses. Two methods of particle refinement have also been examined, in order to increase the accuracy near the point of impact. Results of the method are compared with experimental and numerical results from literature, showing good agreement.

1 Introduction

Boats traveling at rough water at high speeds experience considerable shock and vibrations. Due to the rough sea surface, the boat hull is pitching, impacting periodically on the water surface (slamming). The impact of a solid body on water can be very short, lasting only several milliseconds [1], during which the pressure distribution on the hull surface changes rapidly. Estimation of the forces on the hull is crucial to determine the hull motion and the loads which the hull should withstand.

Simulation of the hull motion may be done in several ways [2]:

– Using a 2D approach in conjunction with the potential flow theory to calculate the forces on the hull, ideally considered as a wedge. This approach is rather simplified, because of approximating the flow as potential flow and because of the simplification of the hull.

P. K. Koukouvinis (✉) · J. S. Anagnostopoulos · D. E. Papantonis
Department of Fluids, School of Mechanical Engineering, National Technical University of Athens,
Heroon Polytechneiou 9, Zografos Campus, 15780 Athens, Greece
E-mail: fivoskouk@gmail.com
Tel.:+30-210-7721077

J. S. Anagnostopoulos
E-mail: j.anagno@fluid.mech.ntua.gr

D. E. Papantonis
E-mail: papan@fluid.mech.ntua.gr

– Using a full 3D model of the hull, solving the Reynolds-averaged Navier–Stokes equations. This method is able to give good results; however, it has an increased computational cost.
– Solving slices of the hull in 2D, simplified as wedges of appropriate geometry. This method was proposed by Lewis [3], but the same logic was used by other researchers, too [4]. This method has the advantage of solving several simplified 2D problems using Navier Stokes equations, instead of solving a considerably time-consuming 3D problem.

Lewis [3] used a commercial mesh-based solver to calculate the wedge impact problem. The computational approach used, involved simulating both phases (air and water) and turbulence effects. In the present paper, an Euler solver will be presented which may be used for solving the 2D hull slices (wedges). The solver is based on the SPH method, which does not require a computational mesh, further simplifying the geometry definition and simulation procedure, while being robust and accurate.

The main advantage of the SPH method is that it is very well suited for highly dynamic problems [5,6], like the wedge impact on the water surface. Since there is no need for a mesh and due to the Lagrangian description, the computational elements follow the flow features, adapting to the flow patterns naturally. Furthermore, it is able to handle moving geometries, without needing special mesh treatments. Moreover, the method does not require any free surface tracking techniques, such as the volume of fluid (VOF) method, used in traditional mesh-based algorithms, significantly simplifying the solution algorithm. All the above characteristics of the SPH method render it an attractive alternative of the traditional mesh-based methods.

Oger et al. [7] have successfully simulated wedge impacts using the SPH method, but used artificial viscosity to stabilize the algorithm. Thus, in the current paper, the SPH–ALE method is used, which relies on the discretization of the inviscid Euler equations in conservative form under an arbitrary Lagrangian–Eulerian perspective, without requiring additional stabilization terms.

Moreover, particle refinement was used in order to properly capture the impact effects. As it will be shown later on, it is beneficial to use a fine resolution at the point of impact, since it enables to estimate the pressure on the wedge surface with higher accuracy. Two different methods of refinement have been tested; one is a smooth transition from coarse to fine resolution proposed by Oger et al. [7], and the other involves a telescopic refinement in a selected region (similar to the method used by Omidvar et al. [8]).

The SPH–ALE method is able to predict accurately the wedge motion for all impact cases simulated, while also providing a reasonable pressure history on the wedge surface.

2 Numerical method

2.1 Introduction to SPH

An important feature of the SPH method is the fact that the method is meshless; Euler equations are expressed using smoothed particle hydrodynamic (SPH) approximations. SPH approximations enable the calculation of the operators appearing in partial differential equations (PDEs), from arbitrary distributions of computational elements—the particles [9]. For example, Eq. (1) may be used to interpolate a function f at a given point i, and Eq. (2) may be used to obtain the derivative of a function. SPH approximations involve application of the kernel function over a radius around point i, on the neighboring particles j. Similar equations may be expressed for the Laplacian [10],

$$< f(\mathbf{r}_i) > = \sum_{j=1}^{N} \frac{m_j}{\rho_j} f(\mathbf{r}_j) W_{ij}, \tag{1}$$

$$< \nabla f(\mathbf{r}_i) > = \sum_{j=1}^{N} \frac{m_j}{\rho_j} f(\mathbf{r}_j) \nabla_i W_{ij}. \tag{2}$$

In the above equations:

– $\mathbf{r}$ is the position vector, i.e., $\mathbf{r}$: $\{x, y\}^T$.
– m_j and ρ_j are the mass and density of particle j, respectively.
– W_{ij} is the value of the kernel function between i and j, and $\nabla_i W_{ij}$ is the value of the derivative of the kernel function, computed with respect to i

The kernel function W plays a very important role in the accuracy and validity of the approximation and it is preferable to satisfy several conditions, such being even, positive, compactly supported etc. [5]. The kernel function used in the current work is the 4th order spline function, suggested by Violeau [11]:

$$W(\mathbf{r}) = A(h^d) \begin{cases} (\|\mathbf{r}\|/h + 2.5)^4 - 5\,(\|\mathbf{r}\|/h + 1.5)^4 + 10\,(\|\mathbf{r}\|/h + 0.5)^4 & 0 \le \|\mathbf{r}\|/h < 0.5 \\ (2.5 - \|\mathbf{r}\|/h)^4 - 5\,(1.5 - \|\mathbf{r}\|/h)^4 & 0.5 \le \|\mathbf{r}\|/h < 1.5 \\ (2.5 - \|\mathbf{r}\|/h)^4 & 1.5 \le \|\mathbf{r}\|/h < 2.5 \\ 0 & 2.5 \le \|\mathbf{r}\|/h \end{cases} \tag{3}$$

where:

– h is the smoothing length of the kernel function, which determines the influence radius of the kernel function and, consequently, the range of interactions.
– $\|\mathbf{r}\|$ is the distance between two interacting particles.
– $A(h^d)$ is a constant term, needed for the normalization of the kernel function. In 2D, for the 4th order spline, it is equal to:

$$A(h^2) = \frac{96}{1199\pi h^2}.$$

2.2 SPH–ALE method

The SPH–ALE method has been initially developed by Vila [12]. The method is based on the expression of the conservative Euler equations using arbitrary Lagrangian–Eulerian (ALE) framework:

$$L_{u_0}(\mathbf{\Phi}) + \nabla \cdot \left(\mathbf{F}_E^l(\mathbf{\Phi}) - u_0^l \mathbf{\Phi}\right) = 0 \tag{4}$$

where:

– $\mathbf{u}_0$ is the transport velocity field, i.e., $\mathbf{u}_0 : \{u_0, v_0\}^T$. If it is equal to the actual flow velocity, Lagrangian description is adopted; if it is zero, then Eulerian description is used.
– L_{u_0} is the transport operator associated with the transport velocity field $\mathbf{u}_0$:

$$L_{u_0}(\mathbf{\Phi}) = \frac{\partial \mathbf{\Phi}}{\partial t} + \sum_{l=1,d} \frac{\partial \left(u_0^l \mathbf{\Phi}\right)}{\partial x^l} \tag{5}$$

with d the number of spatial dimensions.
– $\mathbf{\Phi}$ is the conservative variable vector: $\{\rho, \rho u, \rho v\}^T$. Density is represented with ρ and flow velocity with $\mathbf{u}$: $\{u, v\}^T$.
– $\mathbf{F}_E^l$ is the flux vector:

$$\mathbf{F}_E^1 = \begin{pmatrix} \rho u \\ \rho u^2 + p \\ \rho u v \end{pmatrix} \mathbf{F}_E^2 = \begin{pmatrix} \rho u \\ \rho u v \\ \rho v^2 + p \end{pmatrix}.$$

– The E subscript represents variables calculated from the solution of the Riemann problem, and superscript l denotes the spatial dimension.

Vila noticed that discretization of Eq. (4) leads to 1D moving Riemann problems, which can be linked to the classical Riemann problem by changing appropriately the space variable. The 1D Riemann problem is solved locally, in the middle of the displacement vector between interacting particles i and j.

Eventually, Eq. (4) leads to the following system of discretized equations:

$$\frac{\mathrm{d}}{\mathrm{d}t}(\mathbf{r}_i) = \mathbf{u}_0(\mathbf{r}_i, t), \tag{6}$$

$$\frac{\mathrm{d}}{\mathrm{d}t}(\omega_i) = \omega_i \sum_{j=1}^{N} \omega_j \left(\mathbf{u}_0(\mathbf{r}_j) - \mathbf{u}_0(\mathbf{r}_i)\right) \cdot \nabla_i W_{ij}, \tag{7}$$

$$\frac{\mathrm{d}}{\mathrm{d}t}(\omega_i \mathbf{\Phi}_i) + \omega_i \sum_{j=1}^{N} \omega_j 2\mathbf{G}_E^l(\mathbf{\Phi}) \cdot \nabla_i W_{ij} = \mathbf{S} \tag{8}$$

where:

- $\mathbf{G}_E^l$ are the Godunov flux vectors of the SPH–ALE equations,

$$\mathbf{G}_E^1 = \begin{pmatrix} \rho_E (u_E - u_0) \\ \rho_E u_E (u_E - u_0) + p_E \\ \rho_E u_E (v_E - v_0) \end{pmatrix} \mathbf{G}_E^2 = \begin{pmatrix} \rho_E (v_E - v_0) \\ \rho_E v_E (u_E - u_0) \\ \rho_E v_E (v_E - v_0) + p_E \end{pmatrix}.$$

- ω is the volume of each computational element, which may be called, for simplicity, as particle, even if it actually represents a moving finite volume [13].
- $\mathbf{S}$ is a source term, added to account for gravity effects in the x and y axis momentum equations,

$$\mathbf{S} = \begin{pmatrix} 0 \\ \rho_i \omega_i g_x \\ \rho_i \omega_i g_y \end{pmatrix}.$$

Equation (6) represents the equation of motion of the particles by the transport velocity field $\mathbf{u}_0$. Equation (7) represents the rate of change of the volume of particles according to the divergence of the transport velocity field. Finally, Eq. (8) actually represents the Euler equations in ALE formalism. Thus, Eq. (8) expands to three more equations; one of them is the continuity equation, and the rest two are the momentum equations on x and y axis.

In order to complete the system of equations, one further relation for pressure p is required. This relation is obtained through an equation of state, assuming the water as weakly compressible. In the current work, the Tait equation of state is used:

$$p_i = k{\rho_i}^{\gamma} - B \tag{9}$$

where:

- $k = \frac{B}{\rho_0^{\gamma}}$.
- $B = \frac{\rho_0 c_0^2}{\gamma}$ is the stiffness parameter of the equation of state.
- ρ_0 is the reference density, for water 998.2 kg/m^3.
- γ is a constant, for water it is set to 7.15.
- c_0 is the speed of sound. The actual speed of sound is rarely used, because it would result in very small time steps. In practical situations, an artificial value is used, approximately equal to ten times the maximum velocity of the simulated problem, ensuring that density variation is less than 1 % [9]. In the simulations presented in the current paper, the maximum velocities were in the range of 10m/s; thus, the speed of sound c_0 was set to 100 m/s. Indeed, it was found that maximum density variation was less than 0.5 %.

With the Tait equation of state, the system of equations is complete and it is possible to perform the time integration using an explicit time marching algorithm.

Viscous and surface tension effects have not been included in the calculations, since the Reynolds and Weber numbers are significantly high, denoting that inertia forces are dominant during the impact. To be precise:

– The Reynolds number for the presented simulations is in the range of 1×10^6–6×10^6, using the wedge width as a length scale.
– The Weber number is in the range of 3×10^3, considering the velocity and the thickness of the water sheet which is formed at the side of the wedge during the impact.

2.3 Riemann problem solution

Ivings et al. [14] derived an exact Riemann solver for the Tait equation of state. However, the exact solver is generally not used in practical situations, since it involves the iterative solution of a nonlinear algebraic equation. Solution of this equation is trivial if it has to be calculated only once, but since the Riemann solver is the heart of the SPH–ALE method, the exact solver should be used at each particle interaction, thus significantly increasing the computational cost. For that reason approximate Riemann solvers are used, which are solved with non-iterative methods. In the current work, the Roe approximate solver has been used, based on the work of Leveque [15] and Toro [16].

2.4 MUSCL treatment

The method presented till now, for the solution of the SPH–ALE equations, suffers from excessive numerical dissipation, due to the fact that the Godunov scheme employed is only first order accurate [16]. Thus, a higher order scheme is required, in order of the method to produce accurate results with a reasonable particle resolution. In the current work, the Monotone Upwind Scheme for Conservation Laws (MUSCL)—Hancock [16] scheme is used. The aim of the high order scheme is to reconstruct the field variables at the interface between particles, using the field variables derivatives, appropriately limited, in order to avoid numerical dispersion.

Practically, for each particle involved in the simulation, forward and backward derivatives are calculated [17], using the following equations:

$$\langle \nabla \mathbf{\Phi}_i \rangle_F = 2 \sum_{X_j > X_i} \omega_j \left(\mathbf{\Phi}_j - \mathbf{\Phi}_i \right) \cdot \nabla_i W_{ij}, \tag{10}$$

$$\langle \nabla \mathbf{\Phi}_i \rangle_B = 2 \sum_{X_j < X_i} \omega_j \left(\mathbf{\Phi}_j - \mathbf{\Phi}_i \right) \cdot \nabla_i W_{ij}. \tag{11}$$

Derivatives calculated from Eqs. (10)–(11) are calculated with respect to the global coordinate system. Using them, slopes are calculated at the interface between the particles, and these slopes are limited using the SuperBee limiter [16]. Eventually, an evolution step is performed [16]. After that, the Riemann problem is solved using the reconstructed data. It is highlighted here that the derivative formulation in Eqs. (10)–(11) is only used for the MUSCL procedure and not in Eqs. (7)–(8); in the latter case, the original formulation in Eq. (2) is used instead.

2.5 Boundary conditions

The SPH–ALE method is able to handle boundaries robustly, by considering the boundary surface elements as the interface between two fluid states. Only one fluid state is known; thus, a Partial Riemann problem has to be solved [13,18,19]; the other state may be deduced from the boundary conditions. Then, the contribution of the surface element has to be added to Eqs. (7)–(8), as follows:

$$\frac{\mathrm{d}}{\mathrm{d}t} (\omega_i) = V_{\text{term}} + \omega_i \sum_{j=1}^{N} s_j \left(\mathbf{u}_0(\mathbf{r}_j) - \mathbf{u}_0(\mathbf{r}_i) \right) \cdot \mathbf{n}_j W_{ij}, \tag{12}$$

$$\frac{\mathrm{d}}{\mathrm{d}t} (\omega_i \mathbf{\Phi}_i) + V_{\text{term}} + \omega_i \sum_{j=1}^{N} s_j 2\mathbf{G}_E (\mathbf{\Phi}) \cdot \mathbf{n}_j W_{ij} = \mathbf{S} \tag{13}$$

where:

– V_{term} is the volume term which appears in Eqs. (7)–(8).
– s_j is the surface of the boundary element interacting with the fluid particle i.
– $\mathbf{n}_j$ is the normal vector to the boundary element pointing away from the fluid region.

From the above, it is obvious that surface elements do not need to have any field values by themselves, since the needed data can be deduced from the fluid particles. However, they have to be included in the derivative calculation for the 1st step of the MUSCL scheme. Thus, it is needed to attribute field values to them, too. Pressure on the surface element j is obtained from fluid particles i through the following relation [13]:

$$p_j = \sum_{i=1,N} \omega_i 2 p_E W_{ij}, \tag{14}$$

then density is calculated through the equation of state.

Forces may be calculated by simply integrating the pressure over the whole surface elements j:

$$\mathbf{F} = \sum_{j=1,N} s_j p_j \mathbf{n}_j. \tag{15}$$

For the rest conserved variables $\{\rho u, \rho v\}$, boundary values are found using Shepard filtering [20], which practically is a weighted average:

$$(\rho u)_j = \frac{\sum_i \omega_i (\rho u)_E W_{ij}}{\sum_i \omega_i W_{ij}}. \tag{16}$$

In cases where there is a symmetry plane, symmetry boundary conditions are imposed by directly mirroring particles and their respective field variables appropriately, with respect to the mirror plane (Fig. 1). For example, in the present case of the wedge impact, where $x = 0$ is assumed as a symmetry axis, the mirror particle j will be generated with respect to particle i with the following field variables:

$$\begin{aligned} x_j &= -x_i & (\rho u)_j &= -(\rho u)_i \\ y_j &= y_i & (\rho v)_j &= (\rho v)_i \\ \rho_j &= \rho_i & u_{0,j} &= -u_{0,i} \\ p_j &= p_i & v_{0,j} &= v_{0,i} \end{aligned}$$

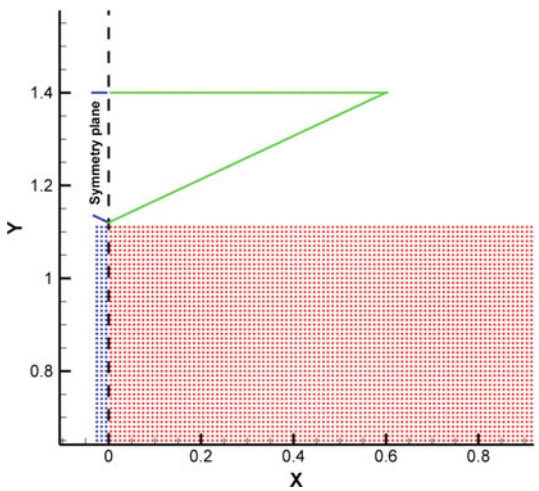

Fig. 1 Particles involved in the simulation: *red* particles are fluid particles, *green* particles are wall particles and *blue* particles are symmetry particles (colour figure online)

3 Simulations and comparisons with experimental data

3.1 Problem description

The problem is very well described in [1,2]. Several test configurations have been tested, and the basic experimental characteristics are the following:

- Wedge top is square, with dimensions 1.2 m × 1.2 m in all cases.
- The deadrise angle θ (see also Fig. 2) of the wedges ranges from 15° to 35° degrees, with an interval angle of 5° degrees. However, experimental data are provided only for the 15°, 20° and 25° angles.
- The wedge impacts the surface after being released from a height of 1 or 1.3 m.
- Adjustable wedge mass ranging from 89 to 158 kg.

The wedge is equipped with pressure sensors at its side, positioned every 50 mm (Fig. 2).

3.2 Simulation parameters

Initially, a particle dependence analysis was performed to determine the appropriate resolution for reproducing the experimental conditions. The particle dependence analysis was performed for a single impact case. The characteristics of the impact are the following:

- Wedge top has a section of 1.2 m × 1.2 m.
- The deadrise angle θ is 25°.
- The wedge is released from a height of $H = 1.3$ m.
- Wedge mass is $m = 94$ kg.

The problem was modeled using the SPH–ALE method, described in the current paper, using three different uniform particle resolutions: 10, 5 and 2.5 mm in order to find the influence of the particle size (particle size dependence study). Symmetry boundary conditions were imposed on the y axis ($x = 0$). Before the impact, the wedge was assumed to be influenced only by gravity. Thus, the wedge was initially positioned just above the water-free surface with an impact velocity of $\sim \sqrt{2gH} = 5.05$ m/s. During the impact, the wedge motion is governed by gravity and pressure forces. The problem is a fluid–rigid body interaction, where the only degree of freedom is the wedge velocity/motion on the vertical axis. The acceleration of the wedge is given by:

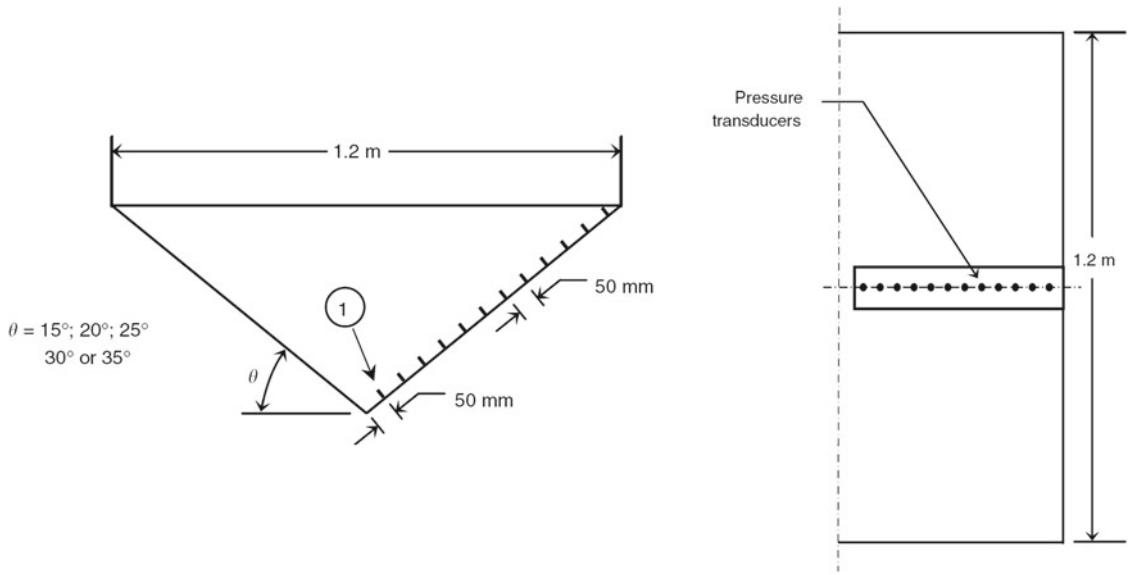

Fig. 2 Wedge schematic [1]

$$a_y = g_y + \frac{F_p}{m_{\text{wedge}}}. \tag{17}$$

Wedge velocity and displacement are obtained by the integration of Eq. (17), which is integrated using an explicit first order method, since the integration time step is imposed by the solution of the Euler equations; thus, it is small enough to ensure sufficient accuracy.

Results for pressure, force and wedge velocity during the impact will be presented in non-dimensional form, using the following conversions:

- Non-dimensional position $x' = x/L_{\text{ref}}$ and $y' = y/L_{\text{ref}}$, where L_{ref} is the wedge width (1.2 m).
- Non-dimensional time $t' = t/t_{\text{ref}}$, where t_{ref} is the total impact time (40 ms).
- Non-dimensional velocity $u' = u/u_{\text{ref}}$, where u_{ref} is the initial wedge velocity, calculated from the drop height $\sqrt{2gH}$.
- Non-dimensional pressure $p' = p/p_{st}$, where p_{st} is the stagnation pressure calculated using the initial wedge velocity just before the impact.
- Non-dimensional force $F' = F/F_{\text{ref}}$, where $F_{\text{ref}} = p_{st}A$ and A is the wedge top surface (1.44 m^2).

3.3 Particle resolution dependence study

Three different particle resolutions have been used, in order to determine the effect of the particle size in the simulation results. The particles size resolution was increased by a factor of two; particle sizes 10, 5 and 2.5 mm, involving 14,000, 56,000 and 220,000 particles equivalently.

In Fig. 3, the wedge v-velocity and the vertical slamming force are shown. From these two graphs, it becomes apparent that the intermediate and fine particle resolutions are able to reproduce practically the same macroscopic results, regarding the wedge motion. Deviation of the wedge vertical velocity between these two resolutions at the end of the simulation is less than 1 %. On the other hand, the coarse resolution (10 mm particle size) calculates the same trends but deviates by ∼5 %. Some differences are found in the vertical force among the different particle resolutions, but generally in all cases the same behavior is reproduced.

The oscillations which appear in the forces graph (Fig. 3), calculated in the finer particle resolution, are probably produced by the pressure wave interaction with the wedge; as the wedge enters the water mass, expanding pressure waves are formed. These waves are quickly dissipated in coarse particle simulations, due to the increased numerical diffusion; thus, in the coarse particle simulation, such oscillations are limited.

A notable observation is that the pressure peaks occur at $t' = 0.5$ and $t' = 0.8$. These peaks are caused by the pressure wave reflection at the tank bottom and the tank corner. Indeed, if one considers the artificial sound speed used (100 m/s) and the distance between the impact location and the tank bottom and tank corner (1.1 and 1.66 m, respectively), the pressure wave reflection would arrive at the impact location at approximately

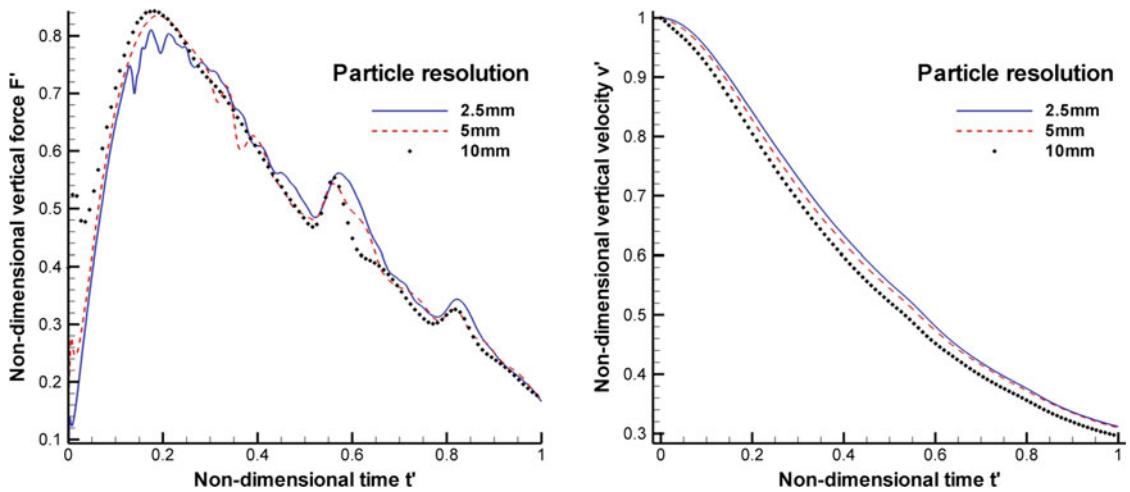

Fig. 3 Results from the particle dependence analysis. *Left* vertical force. *Right* vertical velocity

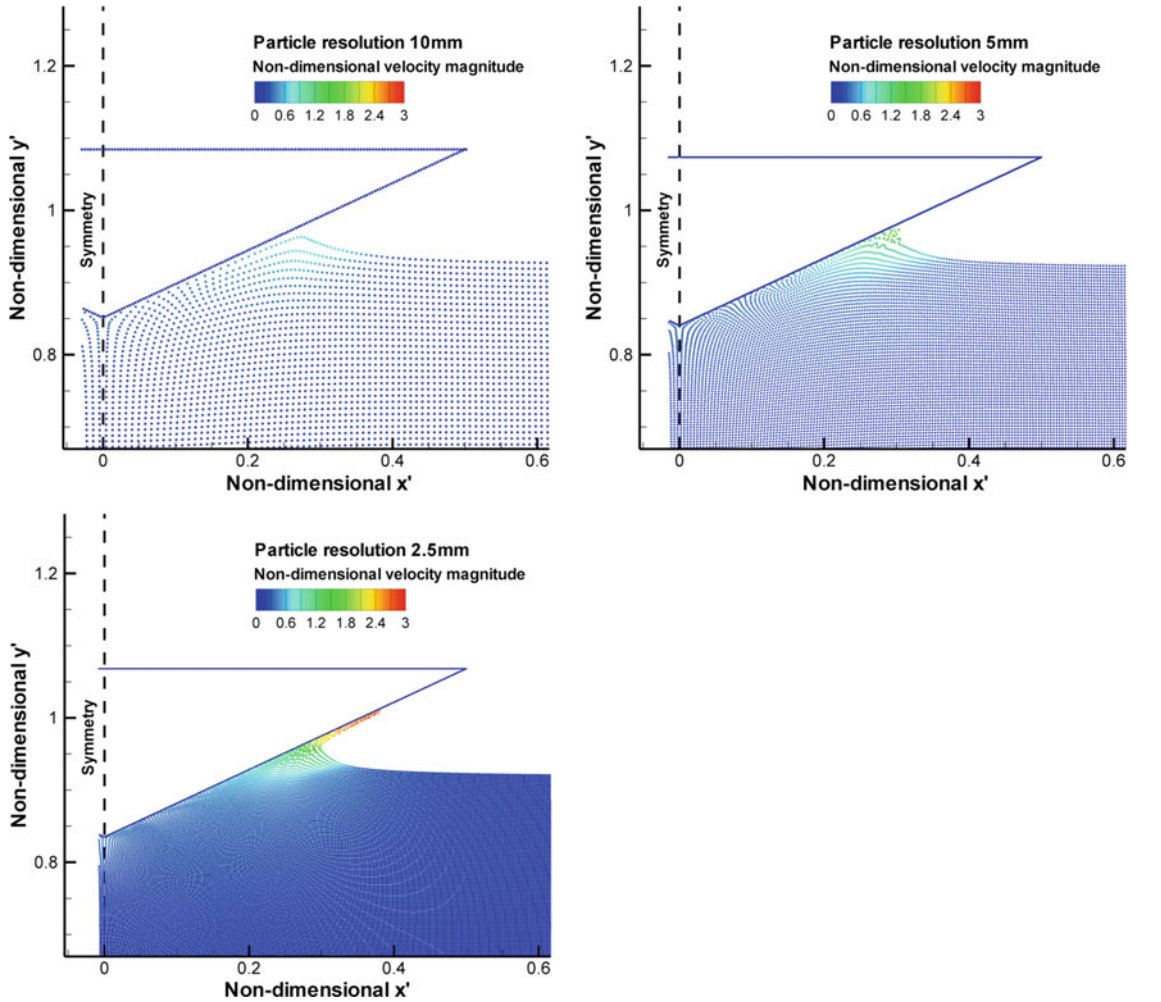

Fig. 4 Indicative results of the wedge slamming for different particle resolutions. Particle coloring according to velocity magnitude

Table 1 Indicative execution times and memory requirements

Particle resolution	Particle number	Execution time (s)	Memory (MB)
Coarse (10 mm)	14,441	280	6
Medium (5 mm)	56,379	3,480	23
Fine (2.5 mm)	222,754	28,400	74

22 and 33 ms, respectively (or $t' = 0.55$ and $t' = 0.83$, respectively), close to what is found in the simulation results. The above underline the capability of the solver to replicate compressibility effects during the impact provided the correct sound speed is used, since water is actually weakly compressible, and such oscillations are found in the experimental results of Yettou [1], too.

In Fig. 4, an indicative view of the wedge slamming is shown, toward the end of the simulation. Even if the macroscopic results of the wedge motion are accurately predicted, some fine details are not properly captured; the water sheet formed on the wedge side is not predicted unless a fine resolution is used. However, even in that case, the resolution of the water sheet might not be adequate, since its thickness is described by ∼4 particles.

The formed water sheet is expected to affect the pressure distribution on the sensors located on the wedge side. Thus, even if the velocity and force results are similar, the fine resolution will be used to obtain the pressure history on the pressure sensors.

In Table 1, indicative execution times and memory requirements are presented for the algorithm to complete the simulation with the three different particle resolutions. The program was executed using 4 parallel threads on an i7-950 (3.0 GHz) processor.

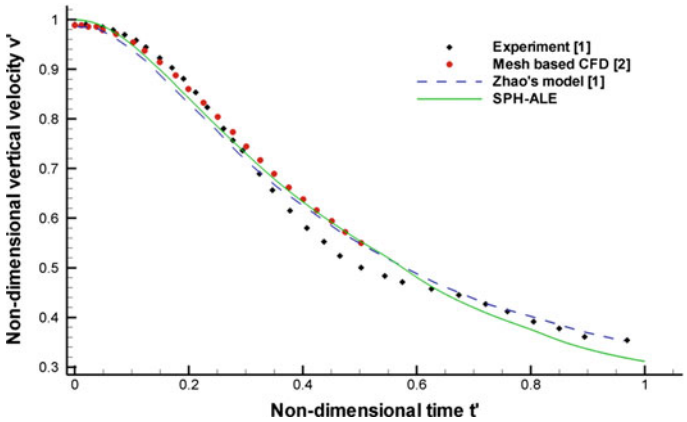

Fig. 5 Wedge vertical velocity

3.4 Comparison of the results with the experimental/literature data

In Fig. 5, the vertical velocity of the wedge is shown, in comparison with experimental data [1], mesh-based CFD results [2] and an empirical model, Zhao's model [1], from the literature. A notable remark is that SPH–ALE does not reproduce accurately the wedge velocity from 13 to 25 ms. The fact that this discrepancy is found in Lewis' CFD results [2] too confirms that it might be caused by 3D effects, which is impossible to capture in a 2D simulation. Indeed, such discrepancies have been experienced by other researchers, too [7].

Nevertheless, numerical results are close, and overall agreement is good. The SPH–ALE method is also close to the analytic model of Zhao, with the exception of a slight velocity underestimation, toward the end of the simulation.

3.5 Pressure sensor results

In this part, the results at the pressure sensors at the wedge side are compared with the experimental results from Yettou et al. [1]. In Fig. 6, the results are shown from transducers 1 to 8. At all pressure transducers, a pressure peak appears at the time of contact of the specific area with the water surface. Since pressure sensors do not come to contact with water all together, but sequentially, one after the other, it is expected to have a lag in the pressure peak. After the peak, pressure gradually reduces.

During the impact, the wedge velocity drops dramatically; indeed, within the 40 ms of simulated impact, the wedge kinetic energy is reduced by ∼88 %. The results show that the greatest pressure peak occurs at the first transducer; this is expected since wedge velocity is approximately equal to the impact velocity. The rest pressure sensors give a smaller peak pressure value, since the wedge velocity reduces with respect to time.

Agreement is very good for the first two sensors (sensors 1–2). Sensors 3–6 underestimate the peak pressure, but the rest pressure history is reproduced satisfactorily. The two last sensors (sensors 7–8) underestimate the pressure values, compared to the experimental data. This is mainly attributed to the rapid dynamics of the water sheet formation/motion and to the insufficient resolution, as it was already discussed in the particle dependence analysis. Further simulations will be performed, using a refined particle resolution near the impact point, in order to properly capture the water sheet and rapid pressure changes.

3.6 Other impact cases

Yettou et al. [1] provided the vertical velocity of the wedge from experimental data and Zhao's model, for several more wedge impacts:

1. Wedge angle 25°, drop height 1.3 m, wedge mass 130 kg
2. Wedge angle 25°, drop height 1 m, wedge mass 130 kg
3. Wedge angle 20°, drop height 1.3 m, wedge mass 89 kg
4. Wedge angle 20°, drop height 1.3 m, wedge mass 143 kg
5. Wedge angle 15°, drop height 1.3 m, wedge mass 143 kg

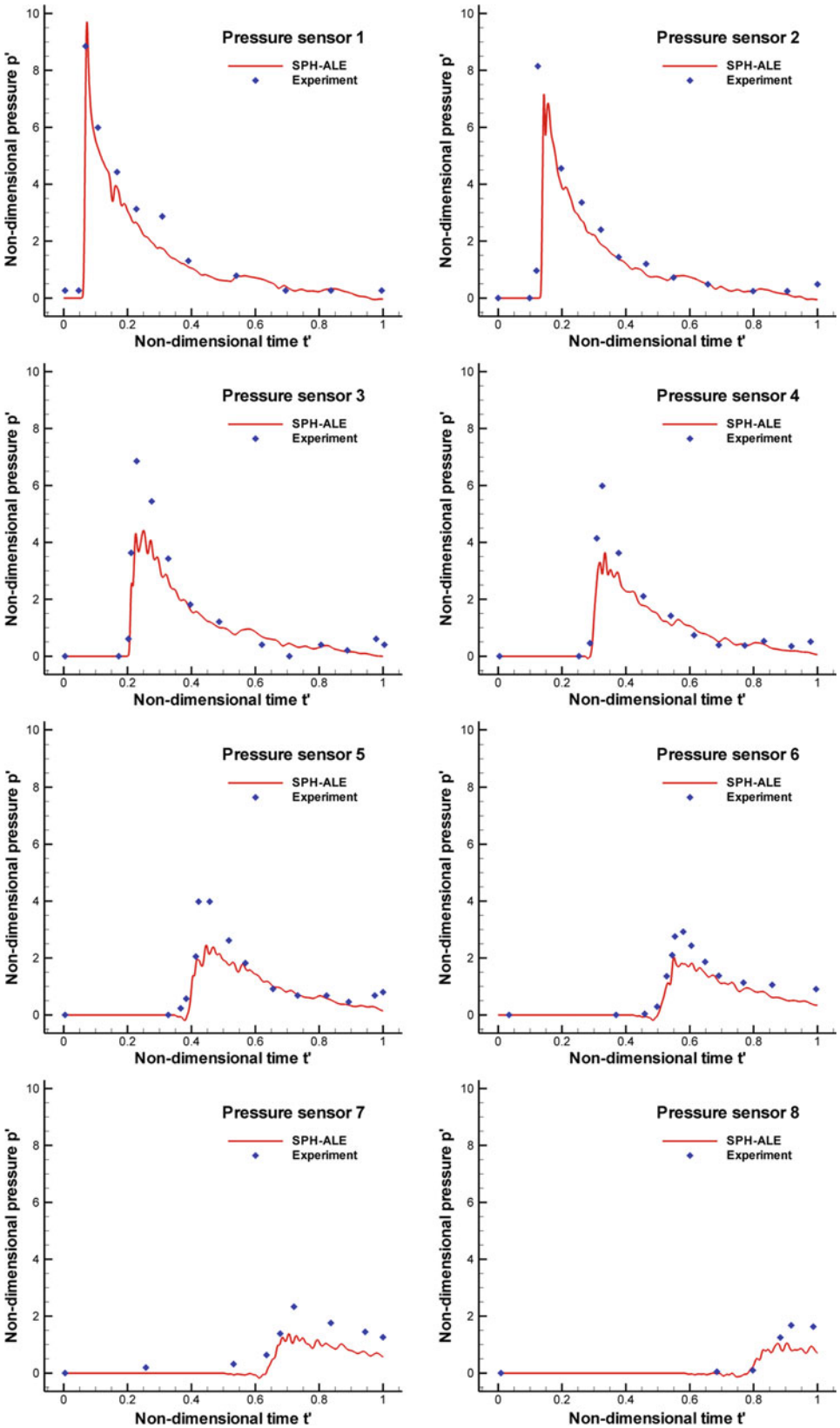

Fig. 6 Pressure history obtained from the pressure sensors at the wedge side

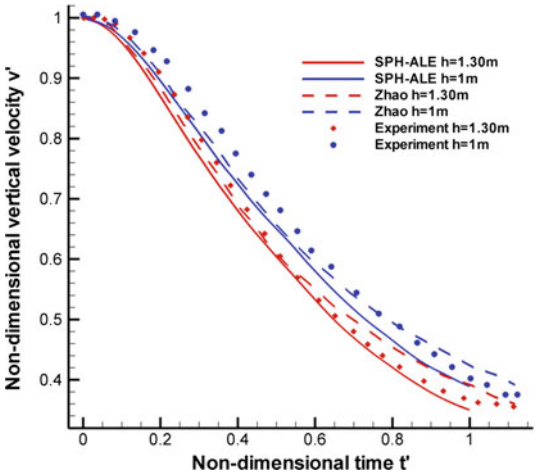

Fig. 7 Wedge vertical velocity during impact. Effect of the impact velocity

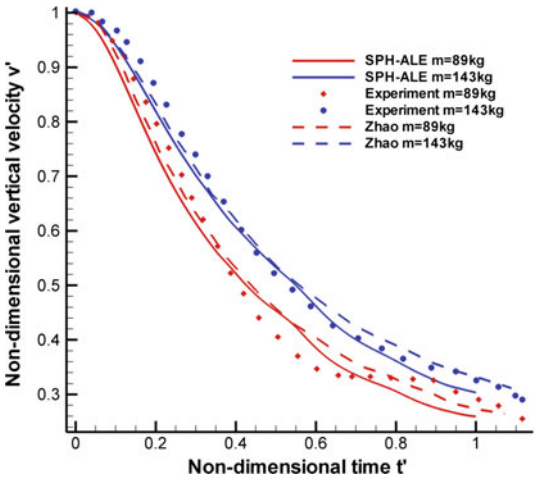

Fig. 8 Wedge vertical velocity during impact. Effect of the wedge mass

These cases have been simulated using a uniform particle resolution of 5 mm, since it was found to be adequate to describe the macroscopic wedge motion. In the following figures (Figs. 7, 8, 9), the vertical velocity with respect to time is shown along with the experimental results and Zhao's model results for each case, respectively. The SPH–ALE method is able to reproduce properly the velocity deceleration during the impact, for all conditions tested.

Figure 7 shows the results for cases 1 and 2. The two cases are identical apart from the drop height, which eventually results in a different impact velocity. Even if the initial impact velocity is different, the final wedge velocity at the ending of the simulation is approximately equal.

Figure 8 shows the results for case 3 and 4, where the influence of the wedge mass is examined. As it is expected, the increased mass of the wedge results in increased wedge inertia and eventually slower deceleration.

Figure 9 shows the results for case 5, where the influence of the wedge angle is examined. Case 5 conditions are the same with case 4 apart from the wedge deadrise angle, which has been reduced to 15°. A smaller wedge angle results in a faster deceleration due to the increased drag.

4 Particle refinement

Further refining resolution uniformly to a particle size of 1.25 mm (which is half of the fine resolution used at the particle dependence analysis) would result in a particle number of ∼850,000 particles. This would result in

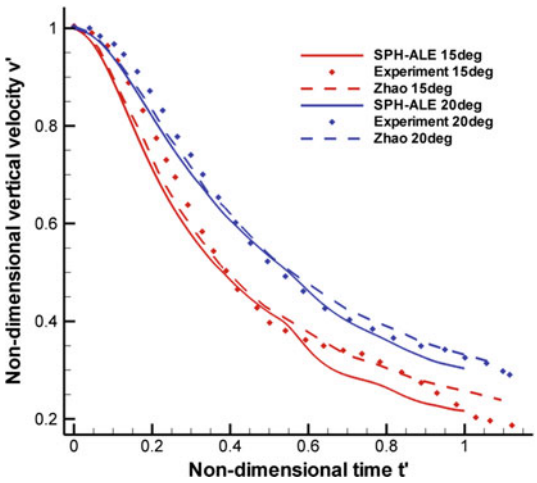

Fig. 9 Wedge vertical velocity during impact. Effect of the wedge deadrise angle

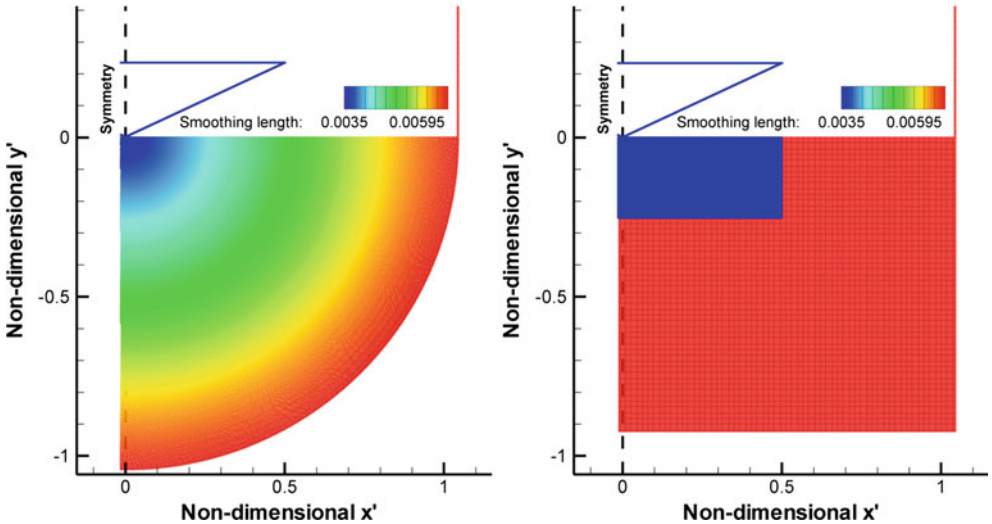

Fig. 10 Refinement patterns. *Left* smooth transition. *Right* telescopic refinement

a very cumbersome simulation, where the increased resolution would be redundant in most areas, since most of these particles would be far from the impact zone. Thus, it is beneficial to use a particle refinement in order to capture the fine details near the impact zone, while keeping the overall particle number to a minimum.

The SPH method is able to handle particle refinement, by adjusting properly the particle size and the smoothing length [5,9]. In the current work, two different particle distributions have been tested. One resembles the distribution used by Oger et al. [7], where particle resolution follows a smooth transition. The other is a telescopic refinement, where particles near the impact zone are split to four smaller particles [8]. The smoothing length in all cases is assumed to be constant in time and equal to $1.4\mathrm{d}x$ where $\mathrm{d}x$ is the particle size. In both cases, particle interactions are kept symmetric using the average value of the smoothing length of the interacting particles, i.e.:

$$h_{ij} = \frac{h_i + h_j}{2},$$

and this averaged smoothing length is used for the kernel function and its derivative calculation.

As a test case, a simulation was performed using both particle refinement methods, in the wedge impact case used for the particle dependence analysis ($m = 94\,\mathrm{kg}$, $\theta = 25°$, $H = 1.3\,\mathrm{m}$). For the smooth transition of particle resolution, the particle size at the point of impact was 2.5 mm, and near the simulated water tank

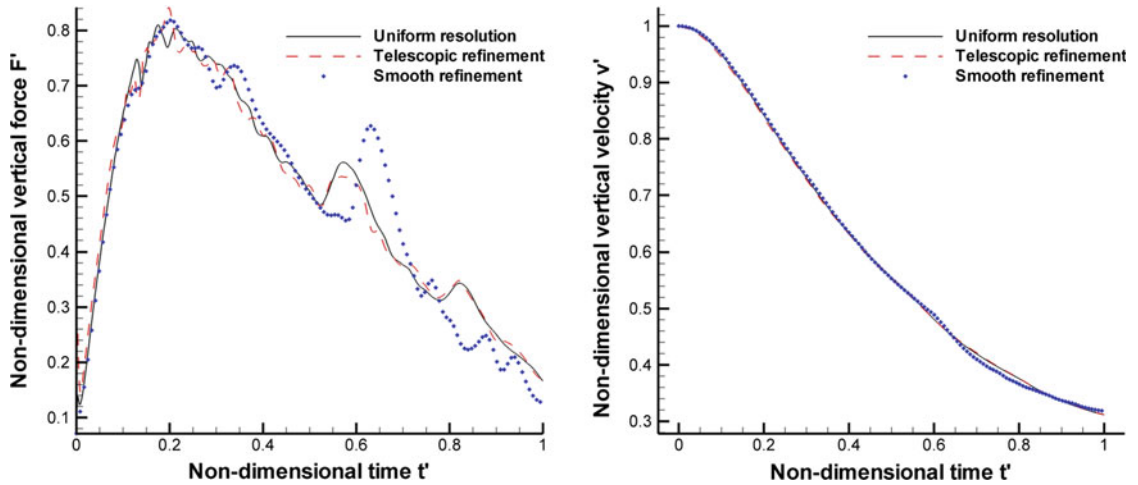

Fig. 11 Comparison of the results of the refinement patterns with the uniform resolution. *Left* vertical force. *Right* vertical velocity

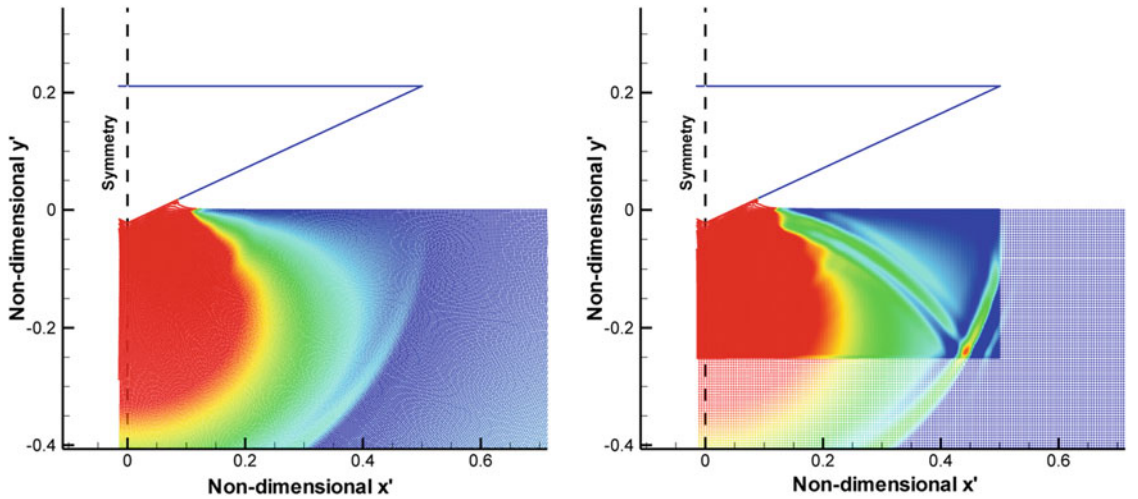

Fig. 12 Pressure field. *Left* smooth transition. *Right* telescopic refinement. Note the pressure wave reflection at the telescopic refinement

boundary 5 mm. Particle size was increased following a geometric sequence with ratio of 1.002. For the telescopic refinement case, all particles had initially a size of 5 mm. Then, particles lying within a square near the impact point were split in four, eventually leading to a resolution of 2.5 mm at the specific zone. Results were compared with the uniform fine resolution (particle size of 2.5 mm everywhere). In Fig. 10, an indicative view of the particle distribution for both cases is shown. Here, it must be highlighted that both refinements lead to a total number of particles ∼80,000, whereas the uniform particle distribution leads to 220,000 particles (fine resolution).

Macroscopic results (i.e., velocity and forces) of the simulations are similar (Fig. 11). However, it is important to highlight that the telescopic refinement causes some artifacts due to the sudden increase in particle resolution. As shown in Fig. 12, pressure waves are reflected at the transition between the low- and high-resolution regions, eventually behaving as a semi-permeable interface. Another important observation is the higher pressure peak at $t' = 0.6$ using the smooth transition; this is the result of using a circular arc to model the tank wall. This tank shape causes pressure wave focusing near the point of impact, which eventually manifests as a single pressure peak, instead of the two peaks experienced with the rectangular tank shape. Moreover, the single pressure peak is delayed by 2.2 ms (or $\delta t' = 0.05$), due to the slightly larger tank size (see also Fig. 10).

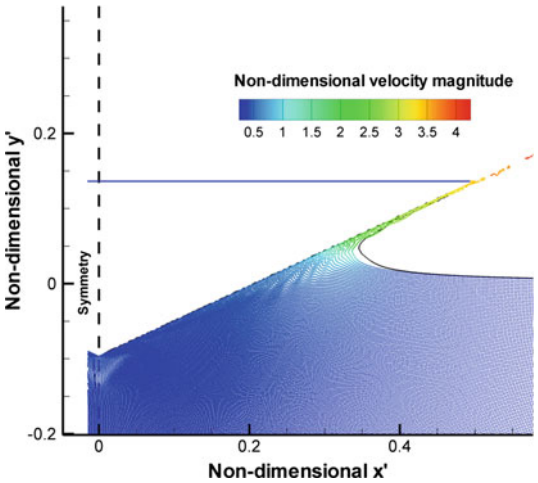

Fig. 13 Free surface comparison of the refined simulation (*colored particles*) and the uniform resolution (*black continuous line*)

The above observations are explained considering Oger's et al. [7] work. Indeed, when variable smoothing length is used, then more terms have to be considered in the derivative calculation formula, such as the gradient of the smoothing length (∇h) and the derivative of the smoothing length with respect to time ($\mathrm{d}h_i/\mathrm{d}t$). The derivative of the smoothing length with respect to time is zero, since the smoothing length does not change throughout the simulation. However, the smoothing length gradient is not zero, and since it was not considered in the SPH approximations used, artifacts appear in areas of sudden smoothing length changes. On the other hand, using a smooth transition minimizes the significance of the gradient term, reducing its effects and enabling the benefits of the particle refinement near the free surface with good accuracy.

4.1 Final results using particle refinement

The previous case was reconsidered using an even higher resolution near the impact point ($\mathrm{d}x = 1.25\,\mathrm{mm}$). Again, near the wall, the particle resolution was 5 mm (growth ratio 1.003). This ratio is small enough to prevent unphysical artifacts. Oger et al. [7] have found that up to a maximum ratio of 1.03, unphysical results are prevented. In Fig. 13, indicative results of the simulation are shown at the end of the simulation: the simulation using refinement is able to capture better the water sheet evolution and the details of the highly curved region. Moreover, the simulation with the 2.5 mm uniform resolution has about two times more particles (∼220,000) than the simulation with refinement (∼120,000).

In the following figure (Fig. 14), the results of the pressure history on the sensors are shown. The simulation with refinement gives results which exhibit some scattering, but tends to predict better the general trend of the pressure history, especially for the last sensors.

5 Conclusion

In this work, 2D wedge impacts on water surface have been analyzed using the SPH–ALE method. The method is based on SPH approximations, which do not require mesh generation and manipulation, while it is able to properly resolve the free surface. Also the method is stabilized by the upwind contribution of the Riemann problem solution, while numerical dissipation is treated using the proven MUSCL–Hancock scheme. Moreover, the ALE description enables proper implementation of boundary conditions in conjunction with the solution of the partial Riemann problem.

Various impact cases have been analyzed; in all cases, the described method was able to produce reasonable results. The wedge velocity history is in close agreement with the experimental data. Discrepancies are minor; however, since such deviations have been reported in similar simulations, (mesh-based or mesh-less) in literature, they are mainly attributed to 3D effects, which are impossible to capture using a 2D simulation. Pressure history on the sensors located on the wedge sides is largely dependent on the formed water sheet

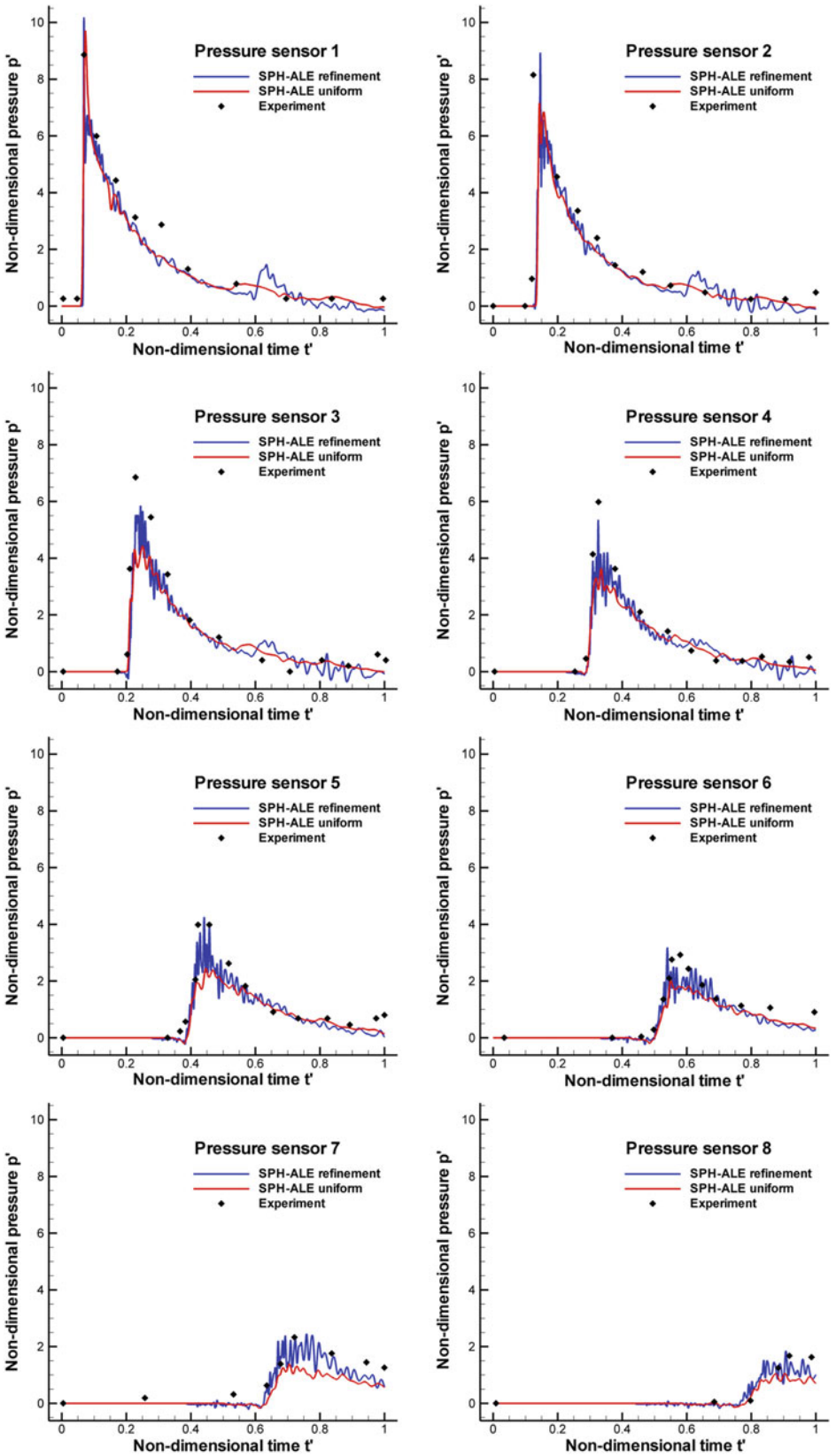

Fig. 14 Pressure history at the pressure sensors. Results for uniform and refined resolutions

description. Simulations employing refinement are able to better capture the water sheet and provide a better pressure history, with respect to experimental data.

Finally, two different refinements have been tested in conjunction with variable smoothing length. Telescopic refinement is problematic, confirming the findings of Oger et al. On the other hand, the smooth resolution transition enables high accuracy with a relatively small number of particles. Results are encouraging to continue using/developing the method in similar cases both in 2D and 3D.

References

1. Yettou, E.M., Desrochers, A., Champoux, Y.: Experimental study on the water impact of a symmetrical wedge. Fluid Dyn. Res. **38**, 47–66 (2006)
2. Lewis, S.G., Hudson, D.A., Turnock, S.R.: Simulation of a free falling wedge into water using 2D CFD with applications in the prediction of high speed craft motions. In: 10th Numerical Towing Tank Symposium, Hamburg, Germany (2007). http://eprints.soton.ac.uk/48788/1/nutts_lewsi07.pdf
3. Lewis, S.G., Hudson, D.A., Turnock, S.R., Blake, J.I.R., Shenoi, R.A.: Predicting the motions of high speed RIBs: a comparison of nonlinear strip theory with experiments. In: Proceedings of 5th International Conference on High Performance Marine Vehicles, Launceston, Australia (2006)
4. Colagrossi, A., Antuono, M., Marrone, S.: A 2D+t SPH model with enhanced solid boundary treatment. In: Proceedings of the 4th Spheric Workshop, Nantes, France (2009)
5. Liu, G.R., Liu M., B.: Smoothed Particle Hydrodynamics: A Meshfree Particle Method, 1st edn. World Scientific Publishing, Singapore (2003)
6. Maruzewski, P., Oger, G., Le Touze, D., Biddisccombe, J.: High performance computing 3D SPH model: sphere impacting the free surface of water. In: Proceedings of the 3rd Spheric Workshop, Lausanne, Switzerland (2008)
7. Oger, G., Doring, M., Alessandrini, B., Ferrant, P.: Two-dimensional SPH simulations of wedge water entries. J. Comput. Phys. **213**, 803–822 (2006)
8. Omidvar, P., Stanby, P., Rogers, B.: Wave body interaction in 2D using smoothed particle hydrodynamics (SPH) with variable particle mass. Int. J. Numer. Methods Fluids **68**, 686–705 (2011)
9. Monaghan, J.J.: Smoothed particle hydrodynamics. Rep. Prog. Phys. **68**, 1703–1759 (2005)
10. Price, D.J.: Magnetic Fields in Astrophysics. Phd thesis, University of Cambridge, UK (2004)
11. Violeau, D., Issa, R.: Numerical modelling of complex turbulent free surface flows with the SPH method: an overview. Int. J. Numer. Methods Fluids **53**, 277–304 (2006)
12. Vila, J.P.: On particle weighted methods and smooth particle hydrodynamics. Math. Models Methods Appl. Sci. **9**, 161–209 (1999)
13. Marongiu J.C., Leboeuf F., Parkinson E.: Riemann solvers and efficient boundary treatments: an hybrid SPHG-finite volume numerical method. In: Proceedings of the 3rd Spheric Workshop, Lausanne, Switzerland (2008)
14. Ivings, M.J., Causon, D.M., Toro, E.F.: On Riemann solvers for compressible liquids. Int. J. Numer. Methods Fluids **28**, 395–418 (1998)
15. Leveque, R.J.: Finite Volume Methods for Hyperbolic Problems, 1st edn. Cambridge University Press, Cambridge (2002)
16. Toro, E.F.: Riemann Solvers and Numerical Methods for Fluid Dynamics: A Practical Introduction, 3rd edn. Springer, Berlin (2009)
17. Koukouvinis, P.K., Anagnostopoulos, J.S., Papantonis, D.E.: An improved MUSCL treatment for the SPH–ALE method: comparison with the standard SPH method for the jet impingement case. Int. J. Numer. Methods Fluids (2012). doi:10.1002/fld.3706
18. Dubois, F.: Partial Riemann problem, boundary conditions and gas dynamics. In: Tourette, L., Halpern, L. (eds.) Absorbing Boundaries and Layers, Domain Decompos. Methods: Applications to Large Scale Computations, pp. 16–77. Nova Science Publishers, New York (2001)
19. Leboeuf, F., Marongiu, J.C.: Application of SPH methods to conservation equations. In: Magoules, F. (ed.) Computational Fluid Dynamics, 1st edn, pp. 87–118. Chapman & Hall/CRC, London (2011)
20. Jang, Y., Marongiu, J.C., Parkinson, E.: Analysis of SPH and mesh based simulations using point based post processing tool. In: Proceedings of the 3rd Spheric Workshop, Lausanne, Switzerland (2008)